

Plastic Deformation Modeling of Foam-Filled Tubes with Multi-Layer Foams During Compression Loading

S. M. H. Mirbagheri*, M. Salehi and A. Jafari Ramiani

School of Metallurgy and Materials Engineering, Amirkabir University of Technology University, Tehran, Iran

ARTICLE INFO

Article history:

Received 12 April 2019

Revised 12 October 2019

Accepted 13 October 2019

Keywords:

Metallic foam
 Multi-layered foam filled tube
 Plastic deformation
 Energy absorption
 Strain hardening

ABSTRACT

The purpose of this paper is to investigate the work hardening behavior and energy absorption characteristic of metallic foams and functionally graded foam filled tubes, including single-, double- and triple-layer foams. Closed-cell A356 alloy and pure zinc foams are fabricated by casting method. The results illustrate that the metallic foams show partially brittle compressive deformation associated with cell walls' bending and tearing. A nonlinear asymptotic model, $\sigma = \sigma_0(1 - \varepsilon)^{-\rho_F/\rho_S}$, is proposed to represent the hardening behavior of metallic foams and graded foam filled tubes as a function of relative density. The development of a complementary model, $\sigma = \sigma_0\varepsilon \sin(n\pi\varepsilon) + \sigma_0(1 - \varepsilon)^{-\rho_F/\rho_S}$, leads to a more accurate estimation of crushing response considering the stress oscillations, particularly for the A356 foam with high degrees of oscillation and multi-layered structures containing distinct plateau regions. Therefore, the present model is fairly consistent with the experimental results. Greater density and strength of the zinc foam compared to those of the A356 foam cause the highest total energy absorption of 581 J in the zinc foam filled tube and the highest specific energy absorption of 459.2 J/(g/cm³) in the A356 foam filled tube. The presence of zinc foam results in the decrease of specific energy absorption. However, it plays a dominant role in adjusting the crash features of graded structures. The compressive properties of multi-layered structures can be controlled by varying the number and material of the layers at constant geometric features.

© Shiraz University, Shiraz, Iran, 2019

1. Introduction

Nowadays, the interest in lightweight materials has been increasing due to the demands of transportation industry [1]. In recent decades, metallic foams, particularly aluminum alloy foams, with an outstanding combination of mechanical and physical properties, have been developed as a new class of functional materials to limit the effect of crashes [1, 2]. Enhanced energy absorption and high specific stiffness have made aluminum foams far more attractive compared to the traditional ones such as dense metals [2, 3]. Generally, closed-cell foams show three regimes of deformation in the compression test. The most important one is the plateau regime, wherein the stress remains nearly constant by increasing the plastic

deformation; thereby, considerable energy is dissipated. Nevertheless, metallic foams reveal a rapid rise in the stress with the minimum increment of deformation in the densification region, and the strain at which this occurs is referred to as densification strain (ε_D). Applications of aluminum foams in many fields call for further insights into the aspect of energy absorption [2, 4, 5]. Moreover, zinc alloy foams are inexpensive, flexible, and exhibit excellent mechanical and damping properties at room temperature. Also, the melting point and strength of zinc alloys are lower than those of aluminum alloys [5-8]. The melt foaming process is one of the most common and economical methods for the fabrication of metallic foams [1, 9, 10].

The common use of thin walled components as the most popular form of crashworthy energy absorbers is

* Corresponding author

E-mail address: smhmirbagheri@aut.ac.ir (S. M. H. Mirbagheri)

due to their specific features, including superior performance under dynamic loading, high efficiency and simplicity of manufacturing and installation. Tubular components such as foam filled square tubes have received noticeable attention in the automobile industry [11-13]. Foam filled structures are often used in mechanical engineering applications as they are cost effective and improve the crashworthiness of vehicles without increasing their weight [2]. The energy absorption of foam filled components is found to be highly dependent on the foam's density and number of pores per inch (ppi). However, filling a thin walled tube, with a high density foam, may lead to a lower specific energy absorption (SEA) compared with the empty tube [11-15].

There is also the chance of controlling the SEA of metallic foams at desired locations by changing the pore structure or type of foam material to obtain a functionally graded foam (FGF). Recently, attempts have been made to fabricate FGFs mainly by varying the pore size and density distribution of the metallic foams. It is desirable that when these FGFs are subjected to compression, first, weaker regions with higher porosity start to deform, and then stronger regions with lower porosity begin to deform. The sequential deformation and plateau stress of graded foams can be controlled at the desired location. It is considered that the lack of reports on the compression properties of FGFs is due to the difficulty of controlling the pore structure in the single foam, particularly in the closed-cell aluminum foam. Therefore, the FGFs, which consist of multi-layers of metallic foams with different properties are expected to exhibit higher functionality than ordinary uniform foams. It has been found that the compressive deformation of these FGFs starts from the foam with lower plateau stress, followed by the foam with higher plateau stress [16-18].

Although some research works are dedicated to modeling the work hardening behavior of metallic foams, a lot of complexity and unknown parameters have still remained. The Hollomon model is not well-fitted with the strain hardening behavior of porous materials such as metallic foams [19]. Therefore, the aim

of this paper is to establish a model for representing the uniform and the oscillation hardening behavior of metallic foams and foam filled tubes under compression loading. To this end, the closed-cell A356 aluminum alloy and pure zinc foams are fabricated and used as core materials for the preparation of single- and multi-layered foam filled tubes. Quasi-static compression tests are carried out on the metallic foams and graded foam filled tubes. Then, an asymptotic hardening model is developed based on the density and strength of porous structures. Also, a comparative study on the crashworthiness is conducted in terms of total energy absorption (E_a) and SEA.

2. Experimental Procedure

Closed-cell metallic foams were manufactured by casting route, as shown schematically in Fig. 1 [21]. The pure zinc and A356 aluminum alloy were melted at 500 °C and 750 °C, respectively. The viscosity of melts was modified by adding 2 wt% of calcium granules at a constant stirring speed of 500 rpm. 1.2 wt% of titanium hydride (TiH_2) powder was added as a foaming agent into the melts at a stirring speed of 1700 rpm. Then, the zinc and A356 alloy melts were poured into cubic steel molds and put into an electrical furnace to allow foam formation at holding temperatures of 600 °C and 700 °C, respectively. Since the decomposition of TiH_2 occurs more slowly in the pure zinc with a lower melting point, longer duration of 12 minutes was selected for its foaming process compared to the A356 alloy with the foaming duration of 3 minutes.

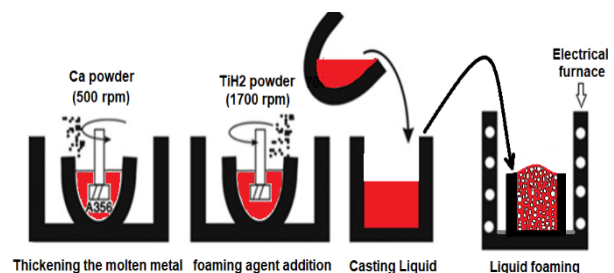


Fig. 1. A schematic of casting route for preparing the closed-cell metallic foams

Square aluminum extrusions with a thickness of 0.65 mm and outer cross section of 24.5×24.5 mm were cut into 51 mm-height tubes. Then, the test specimens were prepared by fitting the foam fillers of different arrangements into the tubes, as shown in Fig. 2. The energy absorbing elements, including the metallic foams, and also, single-, double- and triple-layered foam filled tubes, were coded as shown in Table 1 by using the letters F, T, Al and Zn for addressing foam, tube, A356 aluminum alloy and zinc, respectively. For example, Al-Zn/FT is the tube filled with two layers of A356 and zinc foams, respectively from top to the bottom.

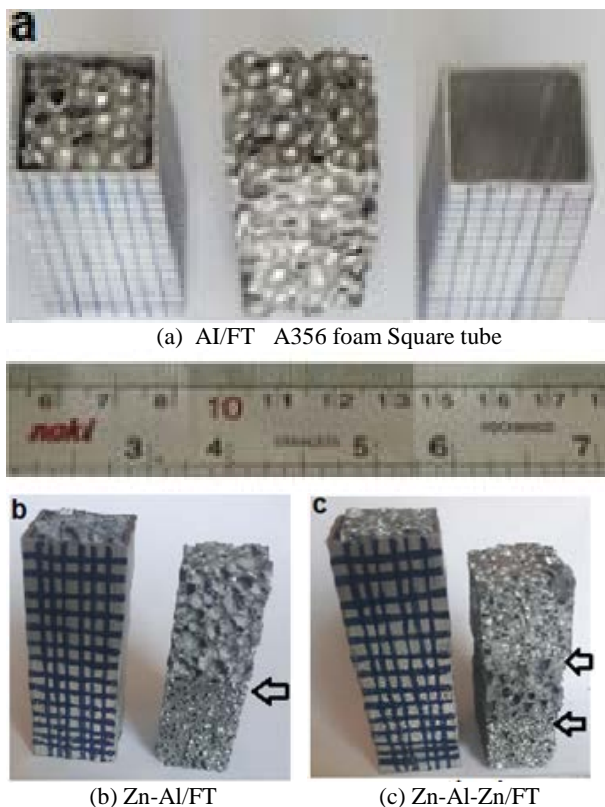


Fig. 2. Arrangement of foam layers in (a) single-layered A356 alloy, (b) double-layered zinc-A356 alloy, and (c) triple-layered zinc-A356 alloy-zinc foam filled tubes

Table 1. Dimensions of foam layers in the energy absorbing elements.

Specimen	Layers \times Height (mm)	Length (mm)	Width (mm)
Al/F	1 \times 51	24.5	24.5
Zn/F	1 \times 51	24.5	24.5
Al/FT	1 \times 51	23.3	23.3
Zn/FT	1 \times 51	23.3	23.3
Al-Zn/FT	2 \times 25.5	23.3	23.3
Zn-Al/FT	2 \times 25.5	23.3	23.3
Al-Zn-Al/FT	3 \times 17	23.3	23.3
Zn-Al-Zn/FT	3 \times 17	23.3	23.3

Uniaxial quasi-static compression tests were conducted at room temperature in a standard universal testing machine (Instron-8502) with a load capacity of 25 kN. A nominal strain rate of $2 \times 10^{-3} \text{ s}^{-1}$ was adopted throughout the tests, and the final crushing displacement was set to approximately 40 mm. The force-displacement data were recorded and plotted by connecting a data acquisition system to the compression testing equipment. The deformation modes of samples were photographed throughout the crushing process, as shown in Fig. 3 for the Zn-Al/FT. The experimental results were employed to develop a mathematical model for predicting the plastic deformation of porous structures. The macrostructure of closed-cell foams and crushed foam filled tubes was observed. Finally, the microstructure of crushed foams in the polished longitudinal sections was investigated by using FESEM.

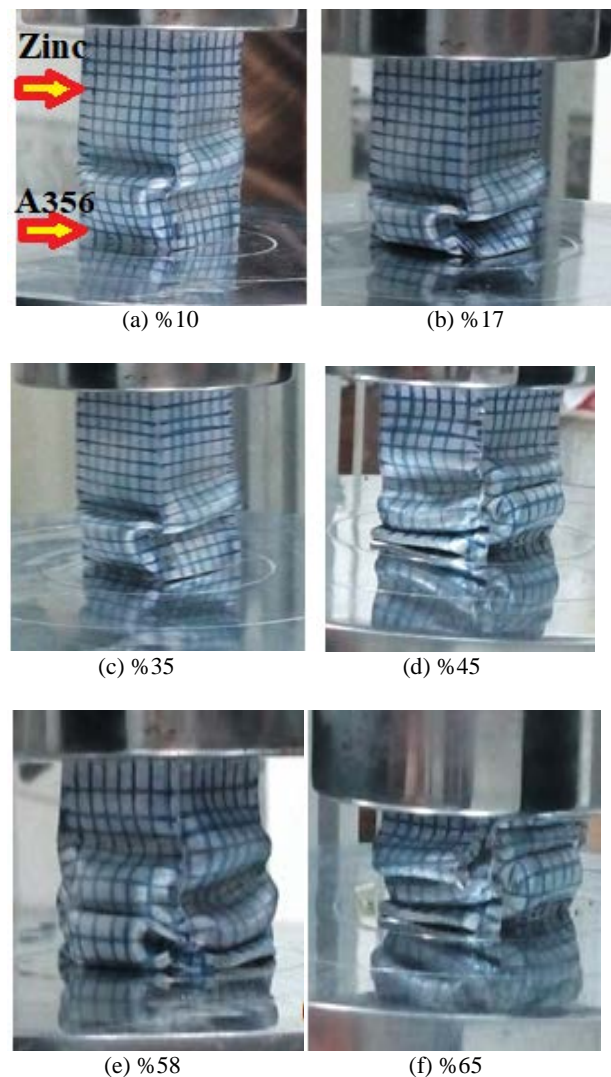
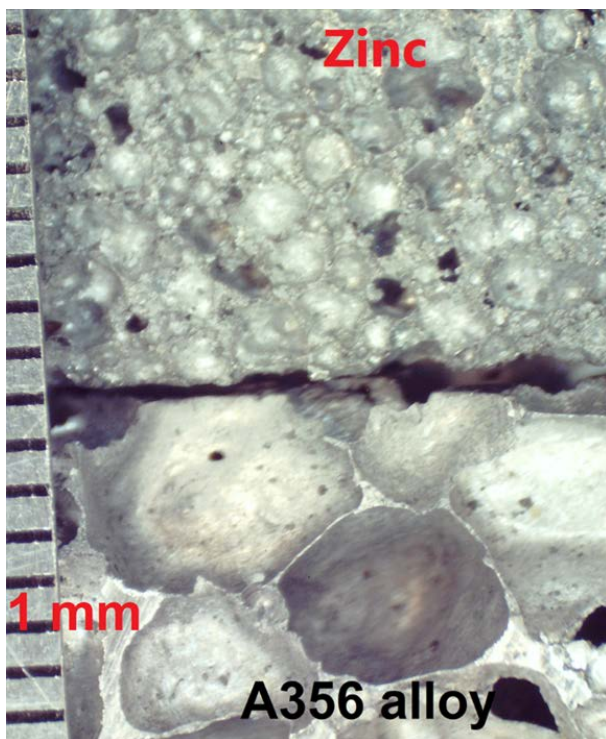


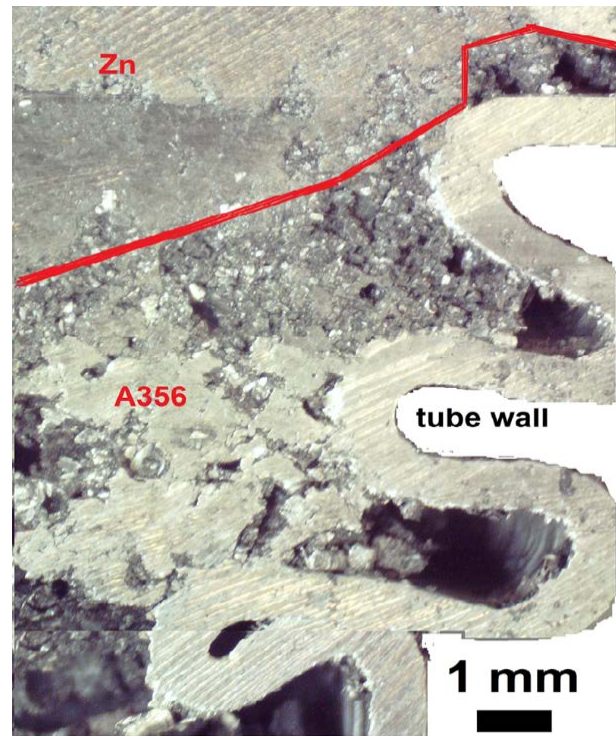
Fig. 3. Sequential images of the crushing process for the zinc-A356 alloy foam filled tube after (a) 10%, (b) 17%, (c) 35%, (d) 45%, (e) 58%, and (f) 65% compression.

3. Results and Discussion

The structure of closed-cell foams consists of solid bubble walls and plateau borders (junctions of two or three bubbles). The macrostructure of Zn-Al/FT before and after the compression test is shown in Figs. 4(a) and 4(b), respectively. According to Fig. 4(a), the A356 foam contains larger size bubbles and thinner cell walls compared to the zinc foam. When the compressive load is applied, bending and fracture of cell edges occur in each foam layer, as seen in Fig. 4(b). Also, the red line in Fig. 4(b) indicates the location of the interface between the crushed zinc and A356 foams. It is generally accepted that the compressive failure of ductile foams is controlled by the cell-edges buckling and cell walls bending, and the compressive failure of brittle foams is governed by the cell edges fracturing and cell walls tearing [1, 5, 8, 20]. Therefore, both the A356 and zinc foams reveal partially brittle mechanisms in the compression test.



Zinc A356 alloy
(a) Before deformation



(b) After deformation

Fig. 4. Macrographs of the zinc-A356 alloy foam filled tube (a) before, and (b) after the compression test.

Figure 5 illustrates the microstructure of Al-Zn/FT after being compressed up to ϵ_D . According to Fig. 5(a), there are many flaky scraps in the A356 foam near the A356/zinc interface caused by the crushing of solid bubble walls. Higher magnification of the crushed A356 and zinc foams near the A356/zinc interface is shown in Figs. 5(b) and 5(c), respectively. It is expected that the fracture of solid bubble walls in the A356 foam layer would happen at the interface of brittle silicon needles and Al (α) solid solution. In other words, the brittle behavior of 356 foam originates from the inherent brittleness of the dual-phase A356 alloy. In the case of zinc foam layer, some micro bubbles can be found in the plateau borders after the crushing of solid bubble walls. In fact, the micro porosities of the cell walls (junctions of two bubbles) are weaker than those of the plateau borders (junctions of three bubbles). Therefore, the brittle fracture and collapse of the zinc foam during the compression test mostly arise from the micro porosities of the cell walls.

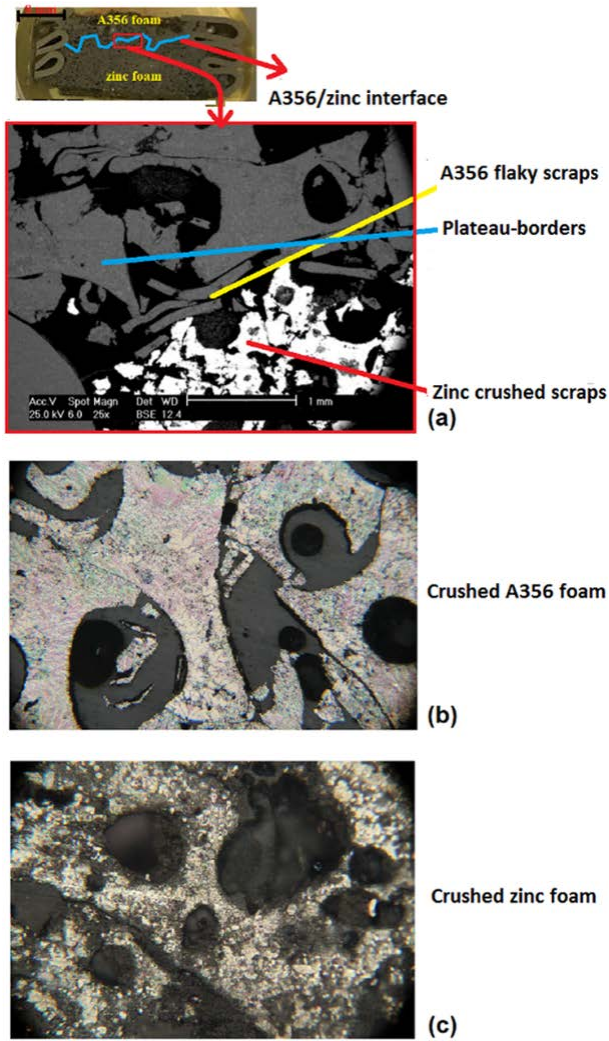


Fig. 5. Microstructure of the A356-zinc foam filled tube after being compressed up to the densification strain, (a) SEM image of A356/zinc interface, (b) optical image of the A356 foam layer near the interface, and (c) optical image of the zinc foam layer near the interface.

In order to investigate the plastic deformation behavior of metallic foams and graded foam filled tubes, as energy absorbing components, the force-displacement and stress-strain curves are plotted under compression loading. In fact, the strain hardening behavior of metallic foams is generally different from that of dense metals. Upon the compression, dense metals do not undergo any changes in volume, mass and density in the plastic stage and follow the power law function ($\sigma = k\varepsilon^n$). However, the Hollomon model cannot fit the compressive data of metallic foams since considerable changes occur in their volume during the plastic collapse [21-23]. Therefore, a nonlinear asymptotic model (mIR model) is developed based on the foam apparent density (ρ_F) and solid

material density (ρ_S) to approximate the strain hardening behavior of metallic foams, assuming that their density increases toward the density of bulk metals during the uniaxial compaction. As a result, the following relationships are achieved by applying the virtual work principle and energy method to the compression test of metallic foams [19, 24-25]:

$$\begin{aligned}
 (l_0 - l + dl) * dF * \rho_S - dF * dl * \rho_S &= F * dl * \rho_F, \\
 \text{and} \\
 (l_0 - l + dl) * dF * \rho_S - F * dl * \rho_F &= dF * dl * \rho_S \\
 \text{and} \\
 (l_0 - l) * dF * \rho_S &= dF * dl * \rho_S - dF * dl * \rho_S + F * \\
 dl * \rho_F &= F * dl * \rho_F \\
 \text{and} \\
 (l_0 - l) * dF * \rho_S &= F * dl * \rho_F \\
 \text{and} \\
 (l_0 - l) * dF &= F * dl \frac{\rho_F}{\rho_S} \quad (1)
 \end{aligned}$$

Where l_0 is the initial length of metallic foams. On the other hand, the parameters φ (compressibility factor) and ε_l (local strain) are defined as follows:

$$\varphi = \frac{\rho_S - \rho_F}{\rho_S} \quad (2)$$

$$d\varepsilon_l = \frac{dl}{l_0}, \quad \text{and} \quad \varepsilon_l = \frac{l}{l_0} \quad (3)$$

Then, the following relationship is obtained by substituting Eq. (2) for Eq. (1):

$$\frac{dF}{F} = \frac{dl}{(l_0 - l)} (1 - \varphi) = \frac{dl/l_0}{(1 - l/l_0)} \cdot (1 - \varphi) \quad (4)$$

Also, by substituting for Eq. (3), Eq. (4) is found as follows:

$$\begin{aligned}
 \frac{dF}{F} &= \frac{d\varepsilon_l}{(1 - \varepsilon_l)} (1 - \varphi) \\
 d \ln(F) &= (1 - \varphi) d \ln(1 - \varepsilon_l) \quad (5)
 \end{aligned}$$

Consequently, the mIR model is identified as the integral part of Eq. (5) from the beginning of the plastic region up to the complete densification, according to Eq. (6):

$$\int_{F_0}^F d \ln(F) = \int_0^{\varepsilon_l} (1 - \varphi) \cdot d \ln(1 - \varepsilon_l) \rightarrow$$

$$\ln\left(\frac{F}{F_0}\right) = (1 - \varphi) \cdot \ln(1 - \varepsilon_l) \rightarrow$$

$$\ln\left(\frac{F/A_0}{F_0/A_0}\right) = \ln(1 - \varepsilon_l)^{(1-\varphi)} \rightarrow$$

$$\sigma = \sigma_0(1 - \varepsilon)^{-\rho_F/\rho_S} \quad (6)$$

Where σ_0 (crushing onset strength) and ρ_F/ρ_S (relative density) represent the strain hardening coefficient (k) and exponent (m), respectively. Regarding nearly similar trends in the crushing response of metallic foams and foam filled tubes [11-15], the present model fits the stress-strain data of graded structures. For this purpose, the equivalent density of layered structures is calculated using the following equations:

$$\rho_{EF} = \frac{\sum_{i=1}^N \rho_{Fi}V_i + \rho_t V_t}{V_t} \quad (7)$$

$$\rho_{ES} = \frac{\sum_{i=1}^N \rho_{Si}V_i + \rho_t V_t}{V_t} \quad (8)$$

Where N is the number of foam layers and V_i is the volume of each layer; ρ_{Fi} and ρ_{Si} are the foam density and solid material density of each layer, respectively. Moreover, ρ_t and V_t are the density and volume of the aluminum tube. Table 2 summarizes the important characteristics of energy absorbers to conduct the hardening model.

Table 2. Characteristics of energy absorbing elements.

Sample	σ_0 (MPa)	ρ_f (g/cm ³)	ρ_s (g/cm ³)	Ppi (in ⁻¹)
Al/F	1	0.54	2.70	8-10
Zn/F	5	2.80	7.10	20-22
Al/FT	14	0.76	2.38	-
Zn/FT	27	2.77	6.59	-
Al-Zn/FT	18	1.76	4.63	-
Zn-Al/FT	15	1.7	4.65	-
Al-Zn-Al/FT	20	1.43	3.99	-
Zn-Al-Zn/FT	30	2.10	5.30	-

It should be noted that the proposed hardening model has an asymptotic nature and convergence toward a unit value, as shown schematically in Fig. 6 for a metallic foam. In fact, for an element with a thickness of dl , the density is ρ_F at the initiation of plastic deformation.

Then, the deformation proceeds progressively, and the density reaches ρ_s at the completion of densification. Consequently, the plastic stress increases exponentially and tends toward an asymptote line based on this modeling approach. In order to make a better clarification of the influence of ρ_F/ρ_S on the crushing response of porous structures, the model-based estimation of stress-strain curves is presented in Fig. 7 for various values of exponent m . For instance, $m = 1$ indicates the maximum density condition, in which the material acts as a dense metal.

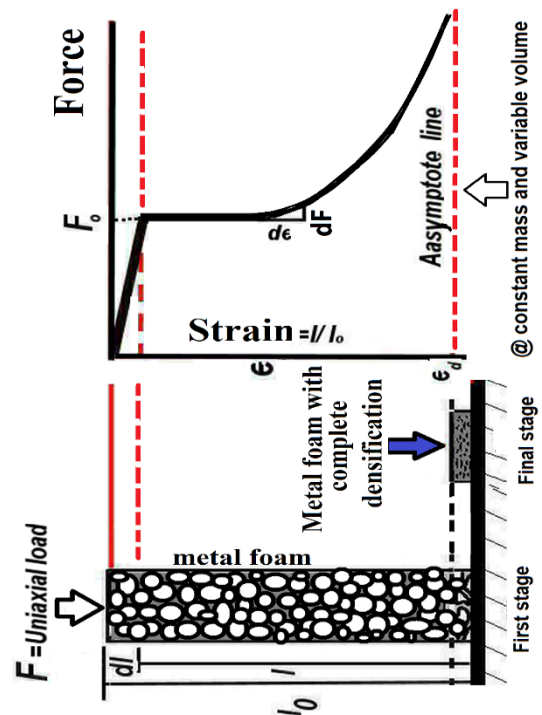


Fig. 6. Schematic of hardening deformation behavior in a metallic foam based on the mIR model.

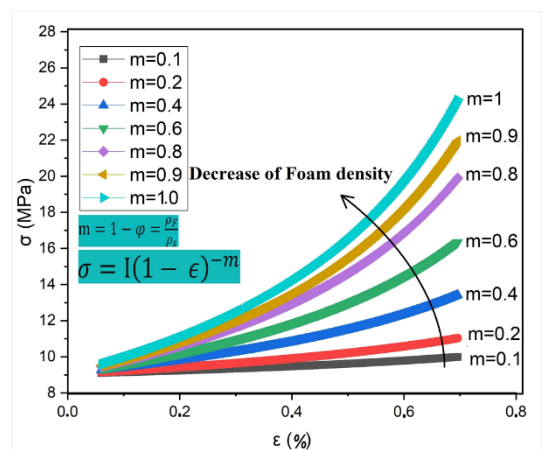


Fig. 7. The model-based stress-strain curves for various values of exponent m .

According to the experimental force-displacement curves and parameters presented in Table 2 for the energy absorbents, the stress versus the strain and $\ln(\sigma)$ versus $-\ln(1-\varepsilon)$ are plotted in the plastic region for both experimental and modeling approaches. Meanwhile, second derivatives of the force-displacement plots are calculated to comprehend the variations of strain hardening rate. Then, the deformation behavior is characterized by the aforementioned plots, as shown in Figs. 8 up to 15 for Al/F, Zn/F, Al/FT, Zn/FT, Al-Zn/FT, Zn-Al/FT, Al-Zn-Al/FT and Zn-Al-Zn/FT, respectively. The force-displacement plots and their second derivatives are illustrated in images (a) and (b), respectively. Images (c) and (e) exhibit the stress-strain plots for the experimental and modeling approaches, respectively. Further, the parameter R^2 in images (d) and (f) represents the coefficient of the determination of the lines fitting the logarithmic plots for the experimental results and mathematical models, respectively.

The compressive force-displacement and stress-strain plots of metallic foams and foam filled tubes can be divided into three regions, namely the elastic, plateau and densification regions, as shown in images (a) and (c) of Figs. 8 up to 11, respectively. The deformation mechanism at the linear elastic stage is the elastic bending of the cell struts and cell walls. The elastic region is followed by yielding and plastic hardening to the initial peak force, which corresponds to the collapse of the weakest cells, and then, by a severe drop in the force, to the plastic plateau stage. At this region, the cells densify, and slight stress fluctuations appear by increasing the displacement over a wide range. Finally, a rapid rise happens in the force with the minimum increment of displacement at the densification stage because the cell walls contact each other. In addition, it can be observed that the presence of the foam filler leads to significantly higher force levels compared with the foam alone, which can be attributed to the interactive effect between the tube wall and the foam filler [2, 5, 8, 12-14].

According to images (a) and (c) in Figs. 12 and 13, the force-displacement and stress-strain plots of double-layered foam filled tubes include two distinct plateau

regions implying the plastic deformation of each foam layer. In other words, first the elastic and plateau regions of low density A356 foam layer appear, then the collapse of high density zinc foam layer starts, as also shown in Fig. 3 for Zn-Al/FT. The same trend can be observed in the crushing curves of Al-Zn-Al/FT, as seen in Fig. 14. The first plateau region corresponds to the crushing of two A356 foam layers, and the second plateau region represents the plastic deformation of middle zinc foam layer. Besides, the multi-layered foam filled tubes reveal apparent peaks in their second derivative curves, which indicates the end of the plastic deformation of each foam layer. In the case of Zn-Al/FT, at first, the applied compressive force cannot be absorbed by the high strength zinc foam layer which is in contact with the movable jaw, thereby being mostly transferred to the A356 foam layer. However, in the case of Al-Zn/FT, first, the crushing force is absorbed by the A356 foam layer which is in contact with the movable jaw. Then, it proceeds to the zinc foam layer [16-18].

Table 3 presents the strain hardening logarithmic equations for the experimental results and mathematical models with their corresponding R^2 values. According to Table 3 and (d) images in Figs. 8 up to 15, there is a linear relationship between the experimental $\ln(\sigma)$ and $-\ln(1-\varepsilon)$ with mean R^2 value of 0.75, except for Al/F ($R^2 = 0.1319$) and Al/FT ($R^2 = 0.2895$). By increasing $\ln(1-\varepsilon)$, the model-based $\ln(\sigma)$ also increases linearly, and high mean R^2 value of 0.92 is obtained, as seen in Table 3 and (f) images in Figs. 8 up to 15. The model validation can be deduced from close coefficients of the logarithmic equations in the experimental and modeling approaches, irrespective of Al/F and Al/FT. In order to evaluate the accuracy of the model better, the $\sigma_{Exp.}$ is plotted against the σ_{Model} for the energy absorbents, as shown in Fig. 16. The proposed model seems to be fairly consistent with the experimental results, except for Al/F, Al/FT and Al-Zn-Al/FT, regarding the acceptable R^2 values of the regression lines (more than 0.7) with the slope being close to 1. Significant deviations for Al/F and Al/FT can be explained by high degree oscillations and scattering in the mechanical properties. Besides, larger oscillations in the crushing curves of A356 foam

indicate its more brittle behavior compared with the zinc foam due to the more crushing of the brittle dual-phase structure in the cell walls, and also, the nonuniform distribution of the coarse bubbles [1, 5, 8, 20]. Moreover, the stepwise increment of stress and distinct plateau regions in the crushing curves of multi-layered foam filled tubes may be responsible for the inaccurate model of Al-Zn-Al/FT. In fact, with the increase in the density, the metallic foams are less susceptible to bending, and the same hardening behavior as in the dense metal can be expected.

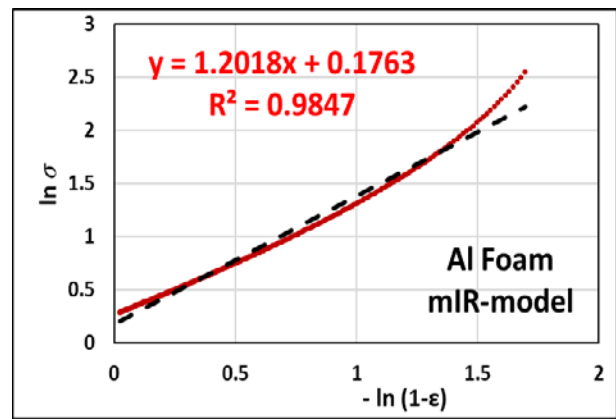
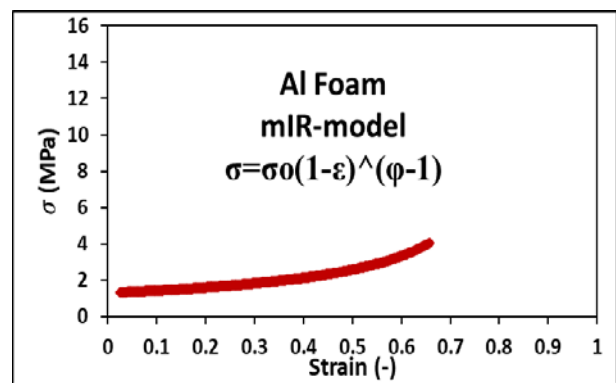
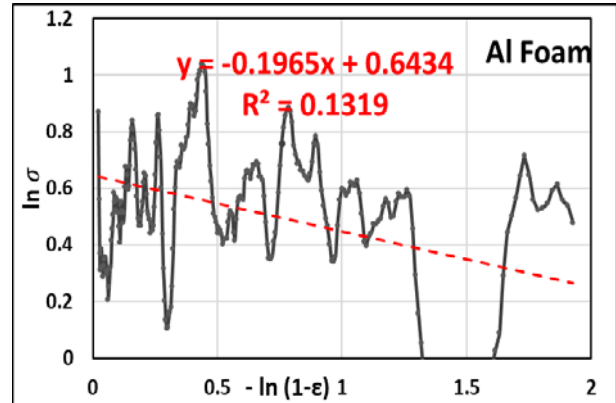
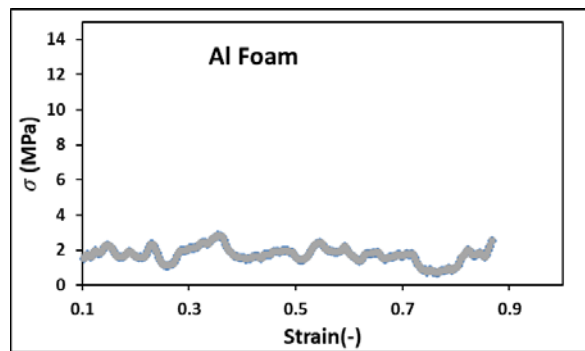
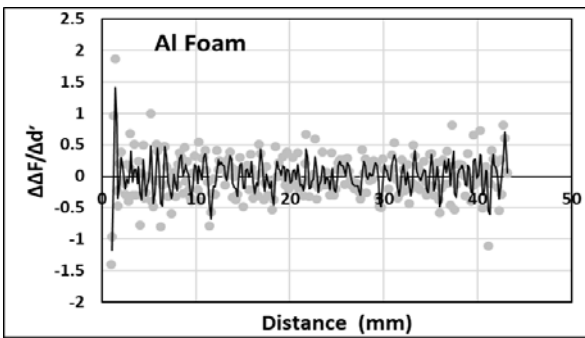
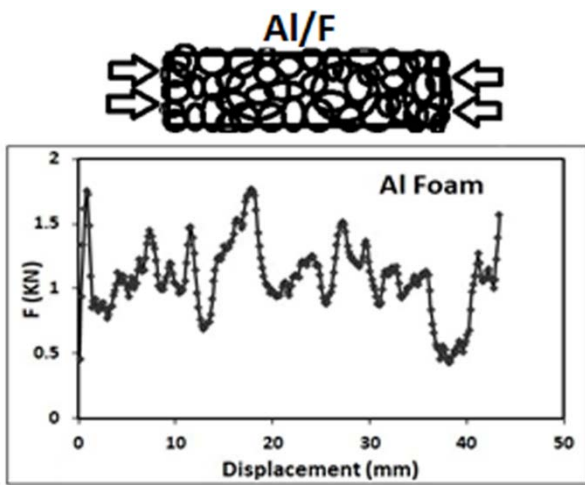


Fig. 8. Uniaxial Plastic deformation behavior of A356 foam, (a) experimental force-displacement, (b) second derivative of experimental force-displacement, (c) experimental stress-strain, (d) experimental $\ln(\sigma)$ versus $-\ln(1-\epsilon)$, (e) model-based stress-strain, and (f) model-based $\ln(\sigma)$ versus $-\ln(1-\epsilon)$ plots.

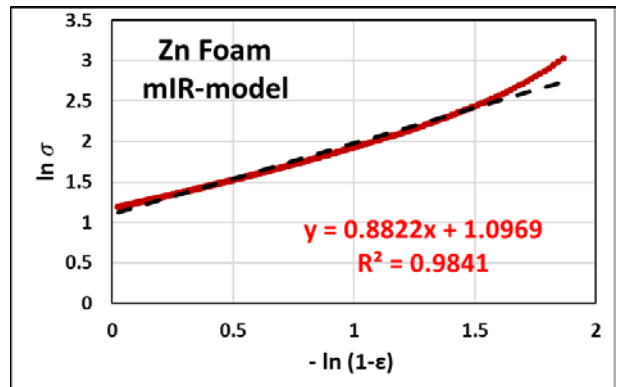
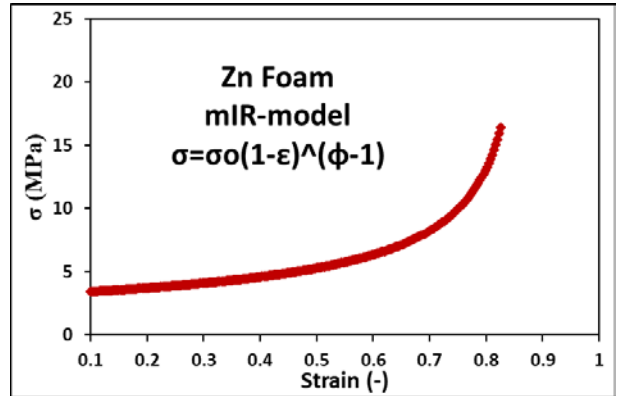
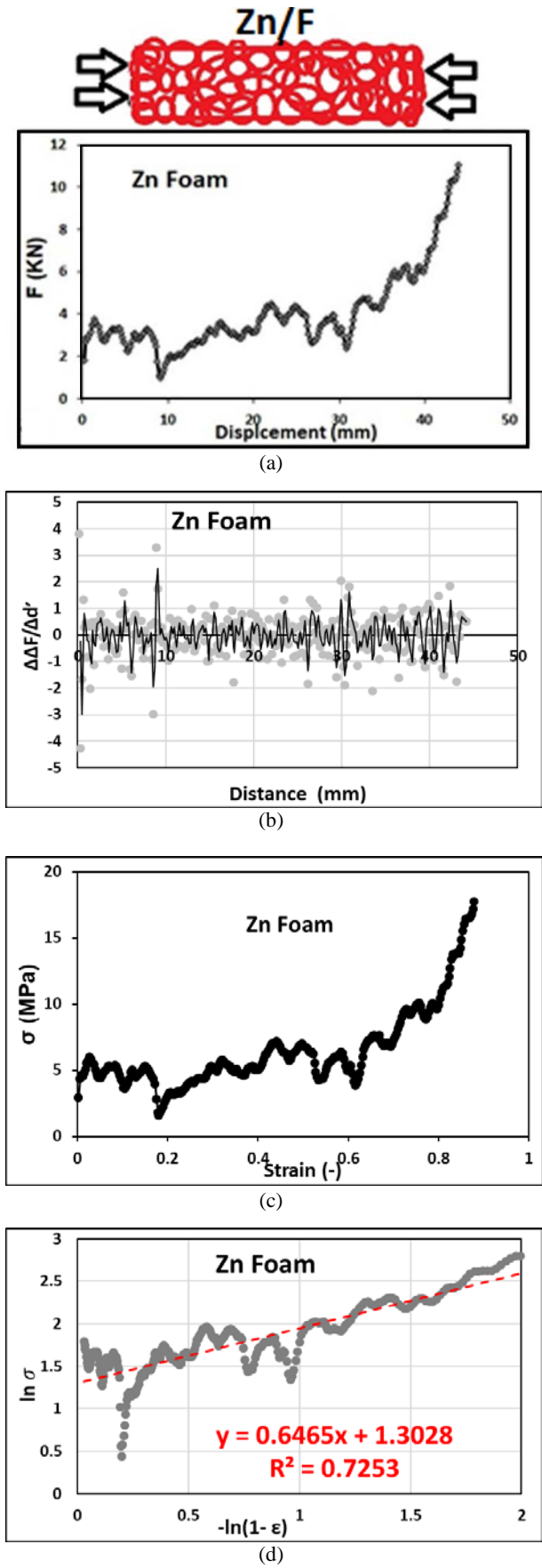
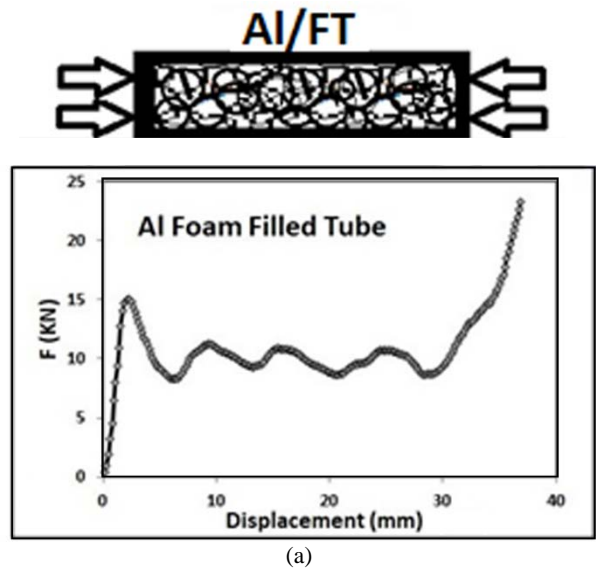
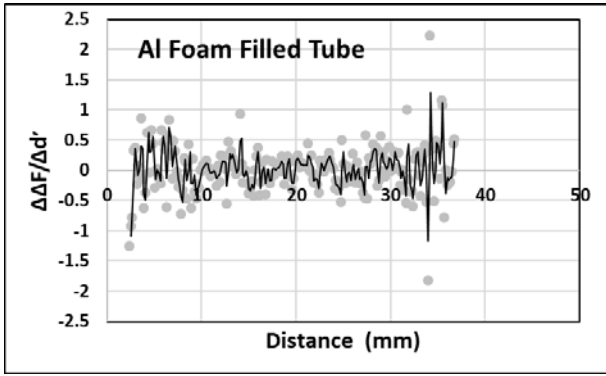
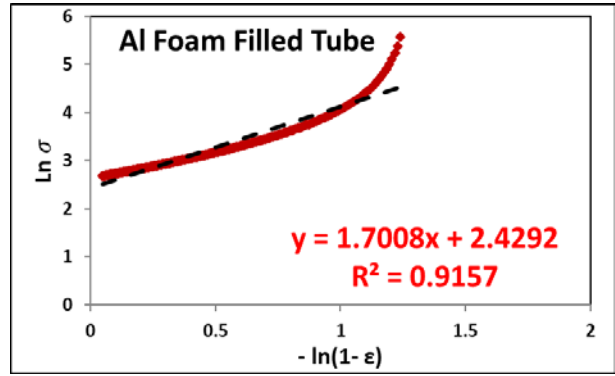


Fig. 9. Uniaxial plastic deformation of zinc foam, (a) experimental force-displacement, (b) second derivative of experimental force-displacement, (c) experimental stress-strain, (d) experimental $\ln(\sigma)$ versus $-\ln(1-\epsilon)$, (e) model-based stress-strain, and (f) model-based $\ln(\sigma)$ versus $-\ln(1-\epsilon)$ plots

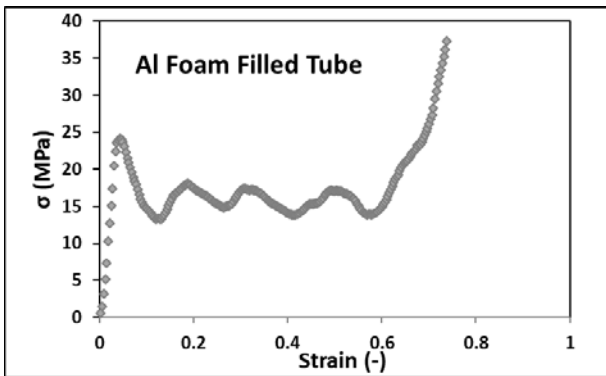




(b)

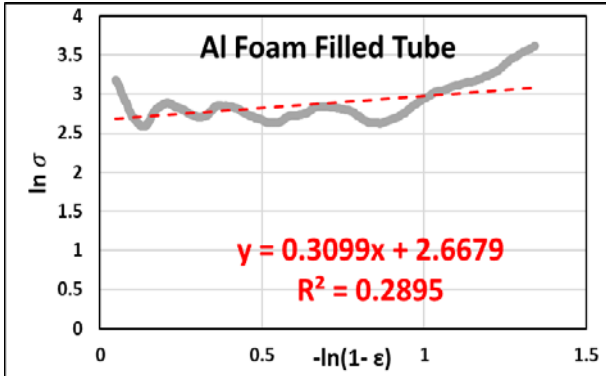


(f)

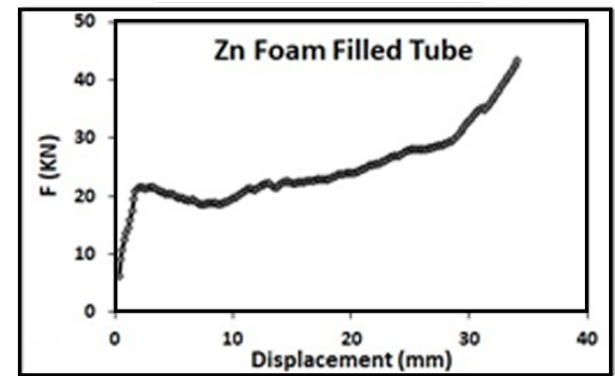


(c)

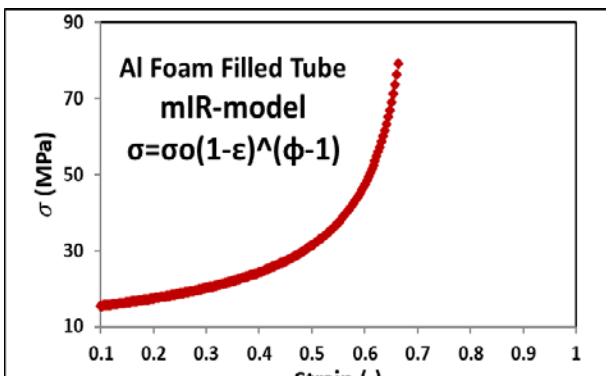
Fig. 10. Uniaxial plastic deformation of A356 foam filled tube, (a) experimental force-displacement, (b) second derivative of experimental force-displacement, (c) experimental stress-strain, (d) experimental $\ln(\sigma)$ versus $-\ln(1-\epsilon)$, (e) model-based stress-strain, and (f) model-based $\ln(\sigma)$ versus $-\ln(1-\epsilon)$ plots.



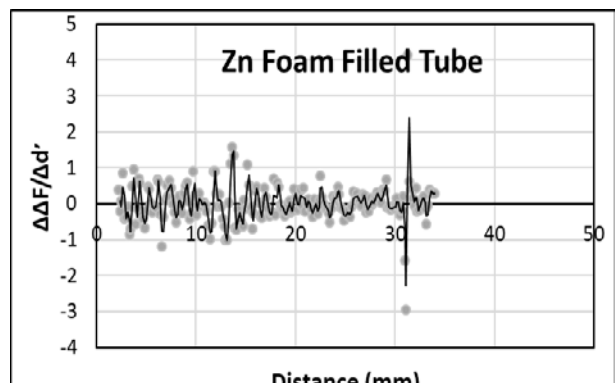
(d)



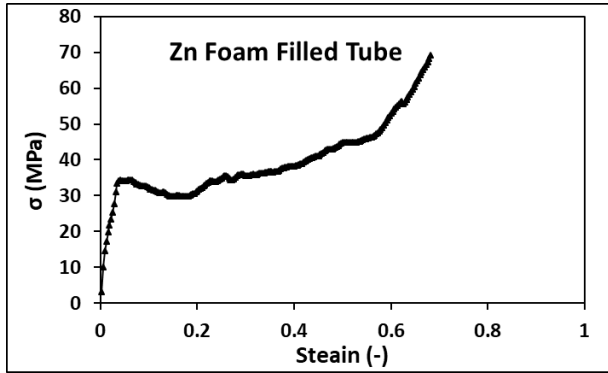
(a)



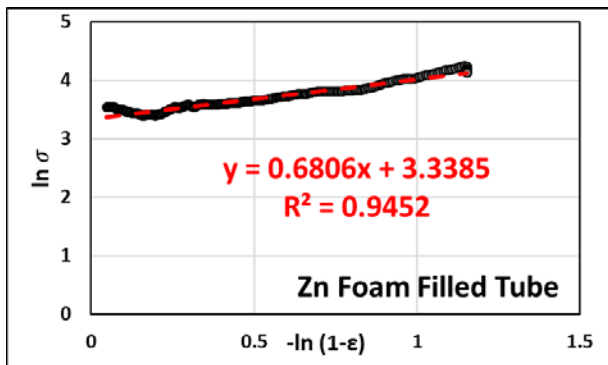
(e)



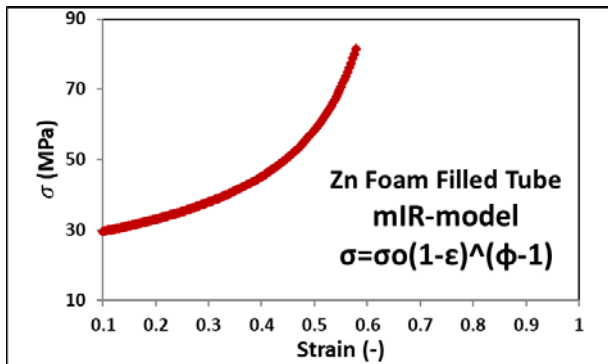
(b)



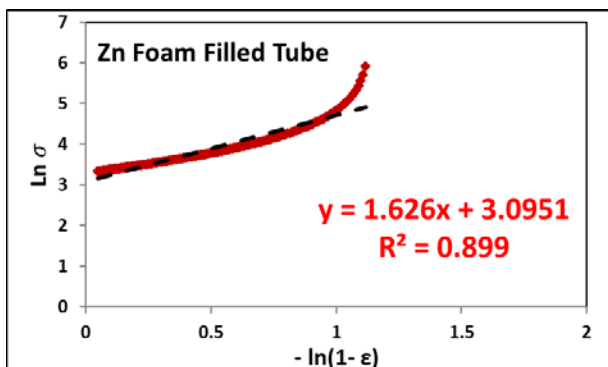
(c)



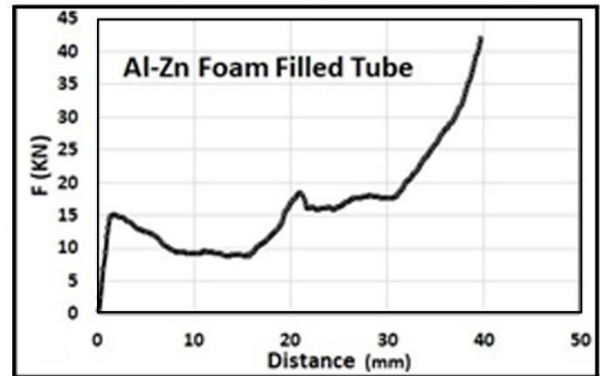
(d)



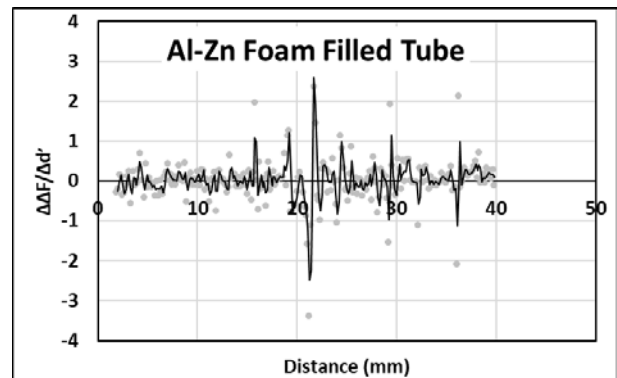
(e)



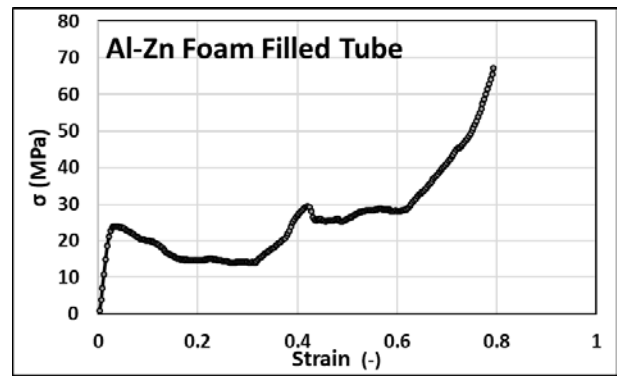
(f)



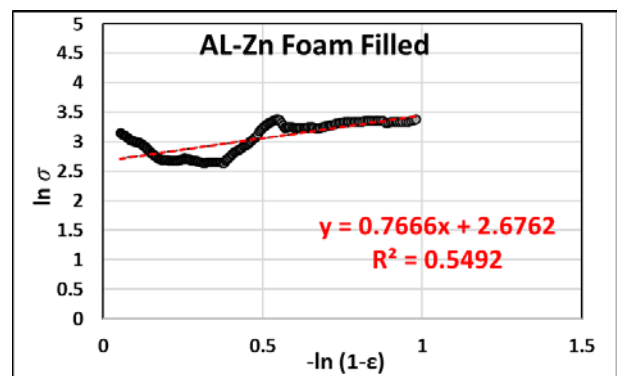
(a)



(b)

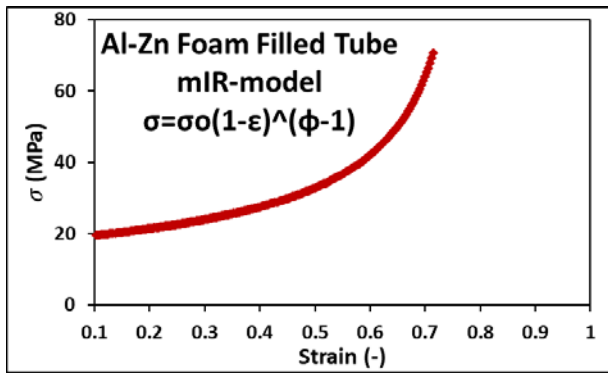


(c)

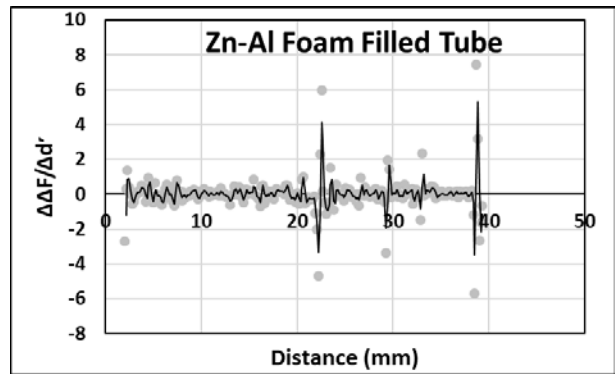


(d)

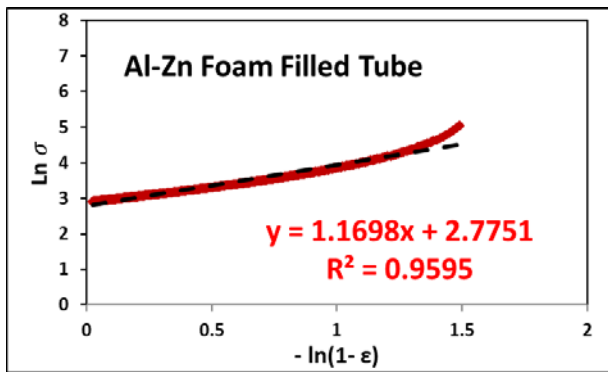
Fig. 11. Uniaxial plastic deformation of zinc foam filled tube, (a) experimental force-displacement, (b) second derivative of experimental force-displacement, (c) experimental stress-strain, (d) experimental $\ln(\sigma)$ versus $-\ln(1-\epsilon)$, (e) model-based stress-strain, and (f) model-based $\ln(\sigma)$ versus $-\ln(1-\epsilon)$ plots.



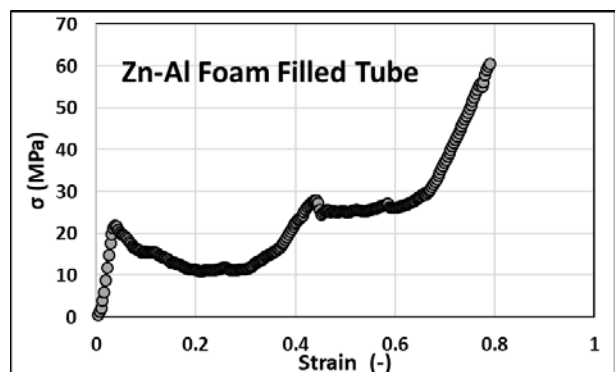
(e)



(b)

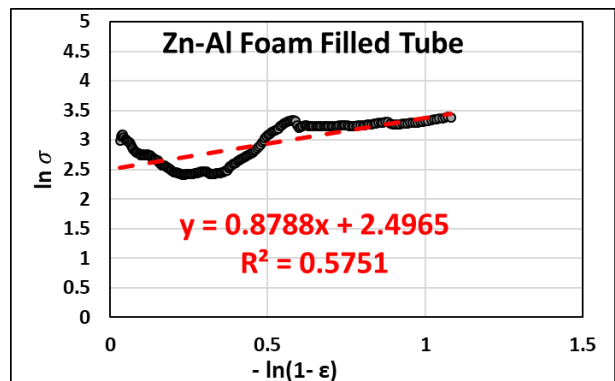


(f)

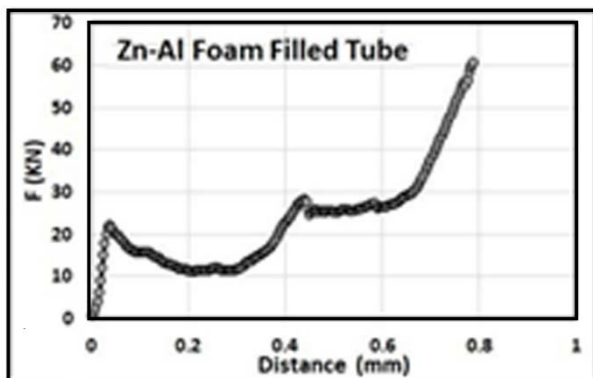


(c)

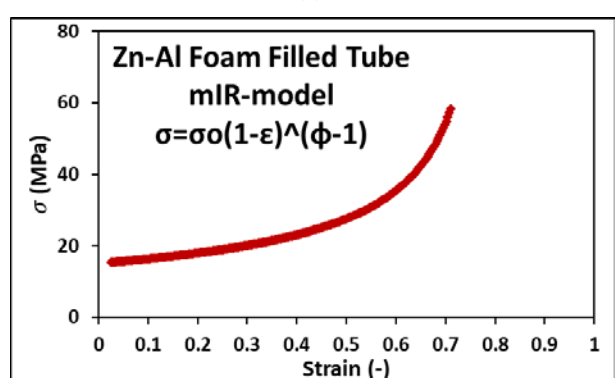
Fig. 12. Uniaxial plastic deformation of A356-zinc foam filled tube, (a) experimental force-displacement, (b) second derivative of experimental force-displacement, (c) experimental stress-strain, (d) experimental $\ln(\sigma)$ versus $-\ln(1-\epsilon)$, (e) model-based stress-strain, and (f) model-based $\ln(\sigma)$ versus $-\ln(1-\epsilon)$ plots.



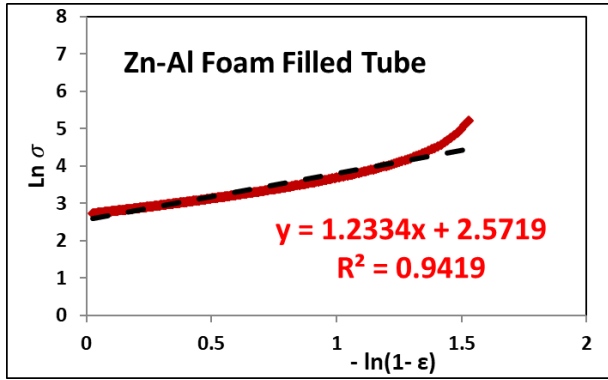
(d)



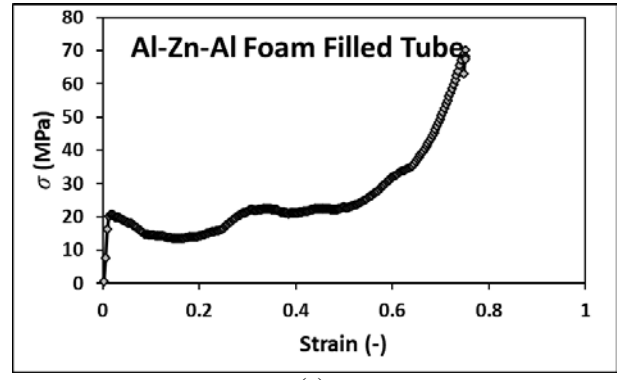
(a)



(e)

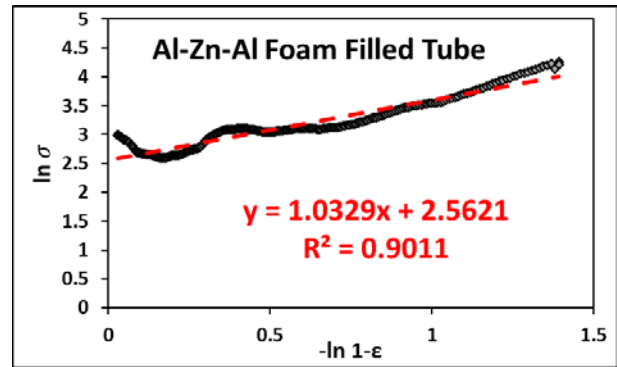
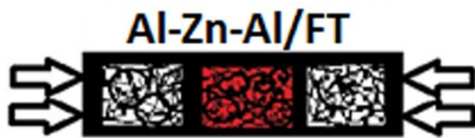


(f)

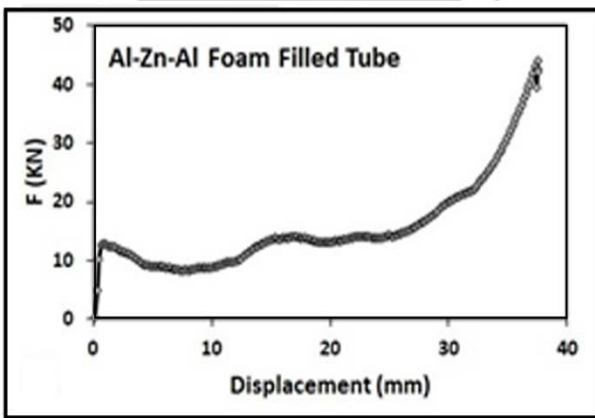


(c)

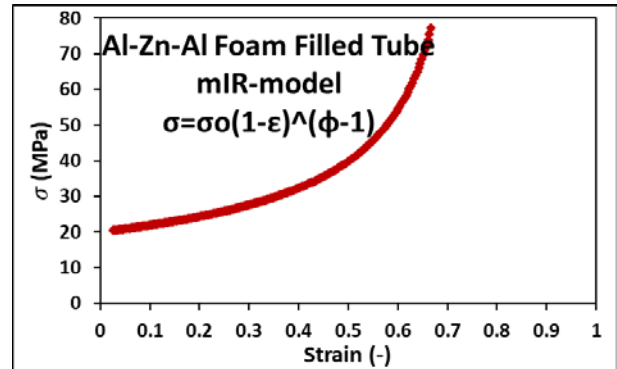
Fig. 13. Uniaxial plastic deformation of zinc-A356 foam filled tube, (a) experimental force-displacement, (b) second derivative of experimental force-displacement, (c) experimental stress-strain, (d) experimental $\ln(\sigma)$ versus $-\ln(1-\epsilon)$, (e) model-based stress-strain, and (f) model-based $\ln(\sigma)$ versus $-\ln(1-\epsilon)$ plots.



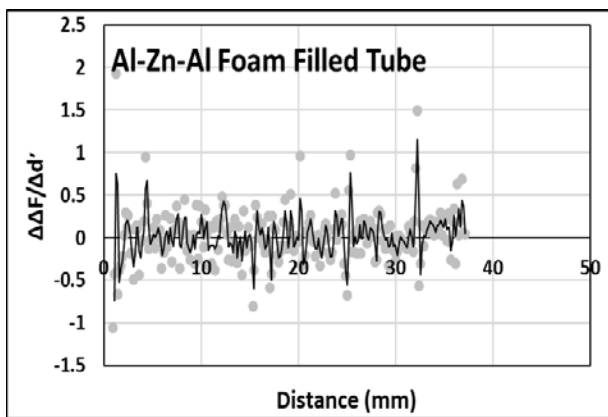
(d)



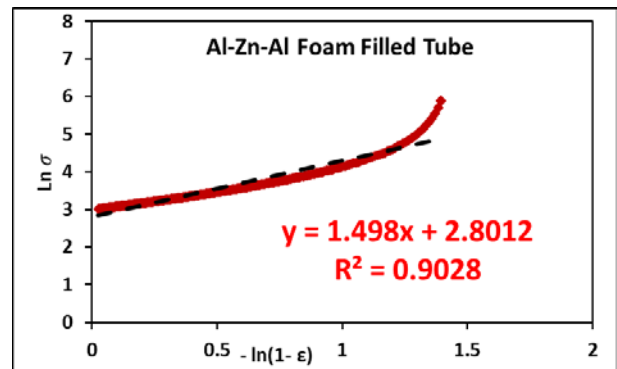
(a)



(e)

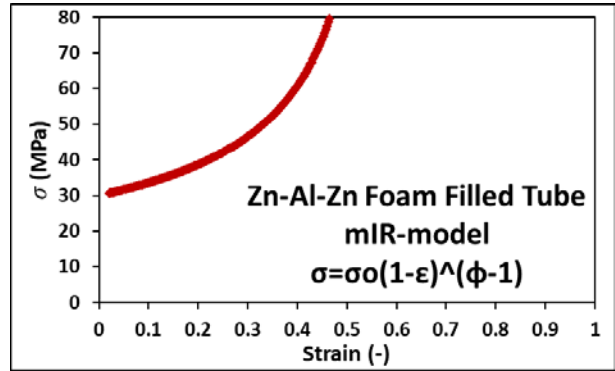
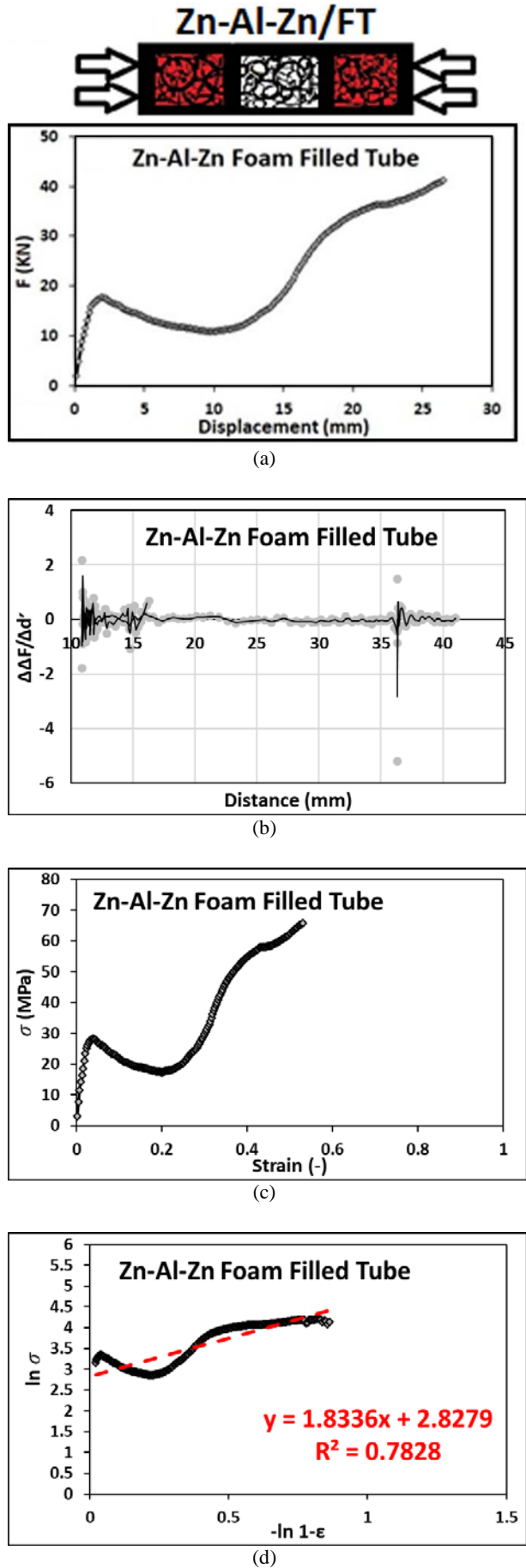


(b)

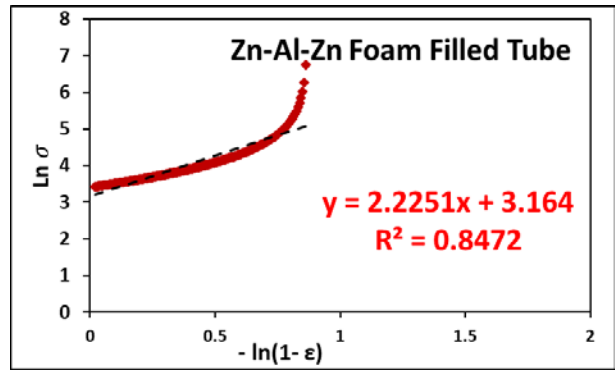


(f)

Fig. 14. Uniaxial plastic deformation of A356-zinc-A356 foam filled tube, (a) experimental force-displacement, (b) second derivative of experimental force-displacement, (c) experimental stress-strain, (d) experimental $\ln(\sigma)$ versus $-\ln(1-\epsilon)$, (e) model-based stress-strain, and (f) model-based $\ln(\sigma)$ versus $-\ln(1-\epsilon)$ plots.



(e)

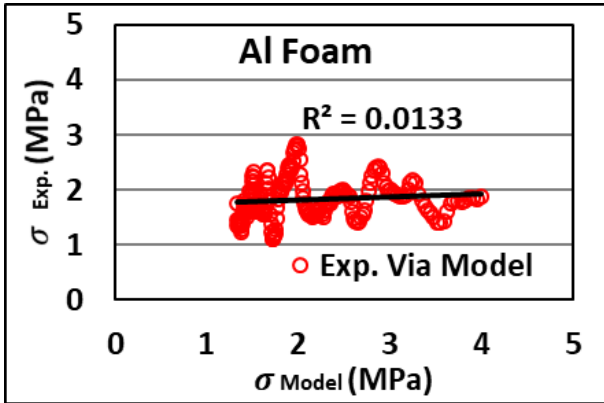


(f)

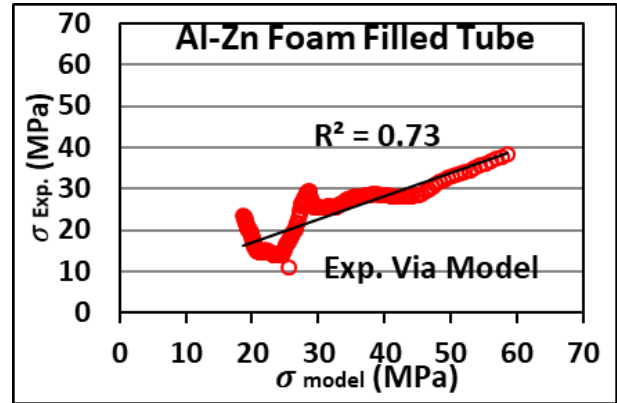
Fig. 15. Uniaxial plastic deformation of zinc-A356-zinc foam filled tube, (a) experimental force-displacement, (b) second derivative of experimental force-displacement, (c) experimental stress-strain, (d) experimental $\ln(\sigma)$ versus $-\ln(1-\epsilon)$, (e) model-based stress-strain, and (f) model-based $\ln(\sigma)$ versus $-\ln(1-\epsilon)$ plots.

Table 3. Strain hardening logarithmic equations for the experimental results and mathematical models

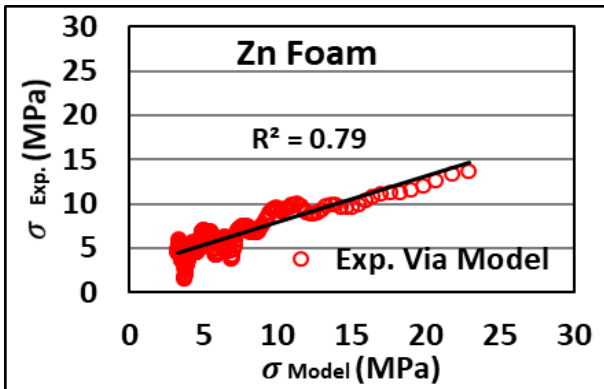
Sample	Experimental Results		Mathematical Models	
	Equations	R^2	Equations	R^2
A356/F	$\ln(\sigma) = +0.1965 \ln(1-\epsilon) + 0.6434$	0.1319	$\ln(\sigma) = -1.2018 \ln(1-\epsilon) + 0.1763$	0.9847
Z/F	$\ln(\sigma) = -0.6454 \ln(1-\epsilon) + 1.3028$	0.7253	$\ln(\sigma) = -0.8822 \ln(1-\epsilon) + 1.3688$	0.9841
A356/FT	$\ln(\sigma) = -0.3099 \ln(1-\epsilon) + 2.6679$	0.2895	$\ln(\sigma) = -1.7008 \ln(1-\epsilon) + 2.4292$	0.9157
Z/FT	$\ln(\sigma) = -0.6806 \ln(1-\epsilon) + 3.3385$	0.9452	$\ln(\sigma) = -1.626 \ln(1-\epsilon) + 3.0951$	0.899
A356-Z/FT	$\ln(\sigma) = -0.7666 \ln(1-\epsilon) + 2.6762$	0.5492	$\ln(\sigma) = -1.1698 \ln(1-\epsilon) + 2.7751$	0.9595
Z-A356/FT	$\ln(\sigma) = -0.8788 \ln(1-\epsilon) + 2.4965$	0.5751	$\ln(\sigma) = -1.2899 \ln(1-\epsilon) + 2.5484$	0.8738
A356-Z-A356/FT	$\ln(\sigma) = -1.0329 \ln(1-\epsilon) + 2.5621$	0.9011	$\ln(\sigma) = -1.4980 \ln(1-\epsilon) + 2.8012$	0.9028
Z-A356-Z/FT	$\ln(\sigma) = -1.8336 \ln(1-\epsilon) + 2.8279$	0.7828	$\ln(\sigma) = -2.2251 \ln(1-\epsilon) + 3.1640$	0.8738



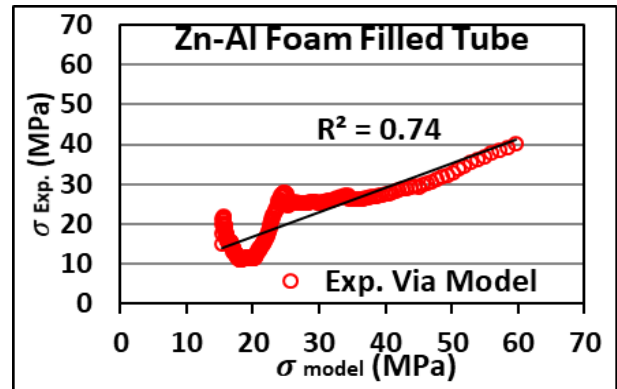
(a)



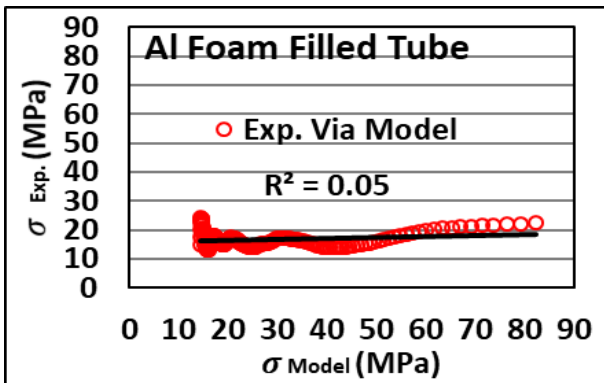
(e)



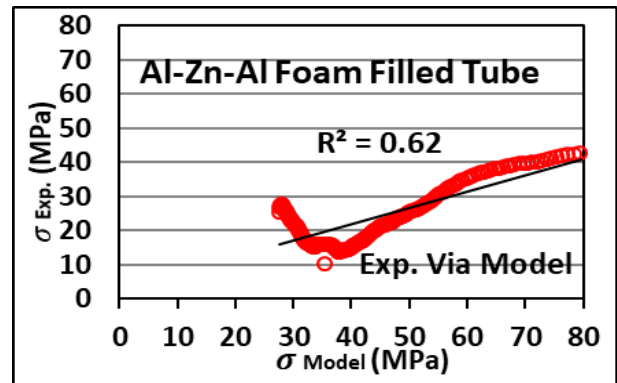
(b)



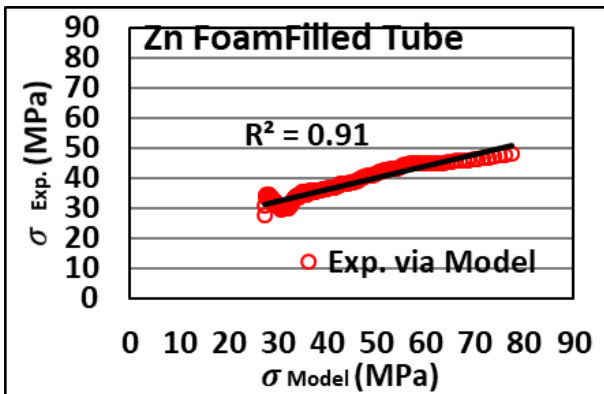
(f)



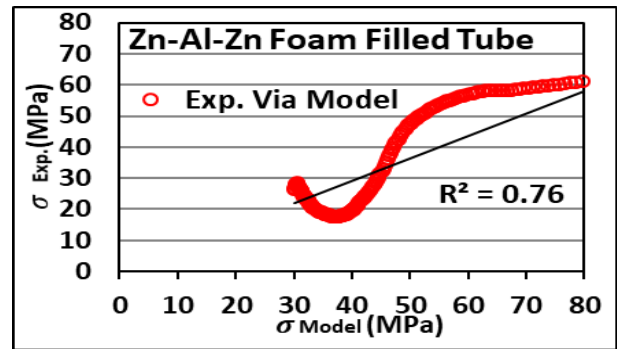
(c)



(g)



(d)



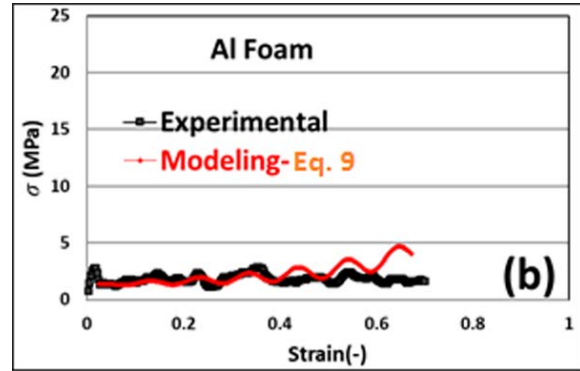
(h)

Fig. 16. σ_{Exp} versus σ_{Model} based on the mIR model for (a) A356 foam, (b) zinc foam, (c) A356 foam filled tube, (d) zinc foam filled tube, (e) A356-zinc foam filled tube, (f) zinc-A356 foam filled tube, (g) A356-zinc-A356 foam filled tube, and (h) zinc-A356-zinc foam filled tube.

In order to take the influence of oscillations on the strain hardening behavior of metallic foams and foam filled tubes into account, a complementary model is developed by adding a sine function to Eq. (6) as follows:

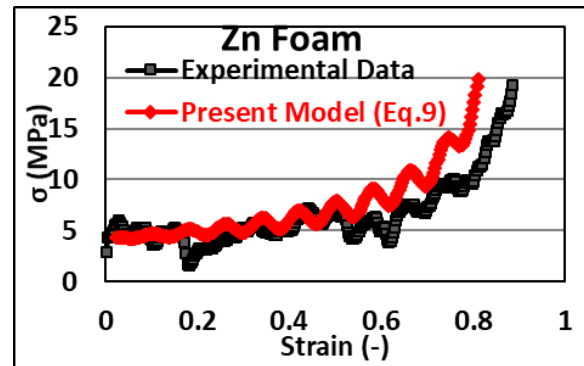
$$\sigma = \sigma_0 \varepsilon \sin(n\pi\varepsilon) + \sigma_0(1 - \varepsilon)^{-\rho_F/\rho_S} \quad (9)$$

Where n is the coefficient indicating the number of oscillations. The complementary model-based stress-strain plots of Zn/F and Al/F are presented in Fig. 17(a) and (b), respectively. In addition, the crushing response of some graded structures, including Al/FT, Zn-Al/FT and Al-Zn-Al with less accurate models, are estimated by applying Eq. (9) to their compressive data. Fig. 18 shows the comparison of the stress-strain plots and stress values between the experiment and the complementary model for metallic foams and mentioned graded structures. It can be observed in the stress-strain plots that the complementary model is in accordance with the experimental results. Furthermore, a linear relationship ($y = x$) between the σ_{Model} and σ_{Exp} with high R^2 values confirms the high accuracy of the complementary model for metallic foams and multi-layered foam filled tubes. Therefore, the plastic deformation of metallic foams and foam filled tubes can be estimated better by the complementary model. To conclude, the oscillation model can be considered as a good substitution for the uniform model (mIR model) to represent the strain hardening behavior of metallic foams and graded structures as a function of ρ_F/ρ_S . However, the present model still needs to be further improvement due to the complex plastic deformation of foam filled tubes.

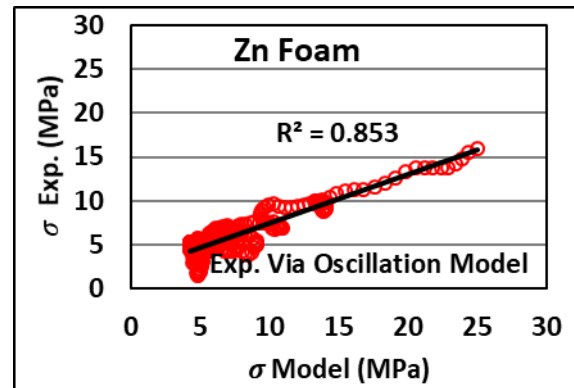


(b)

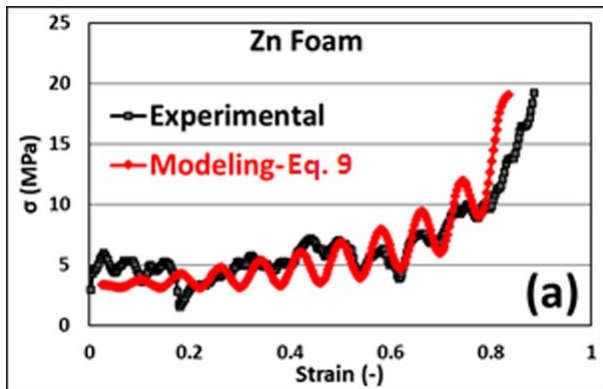
Fig. 17. Comparison of the stress-strain plots between the experiment and complementary model for zinc foam, and (b) A356 foam.



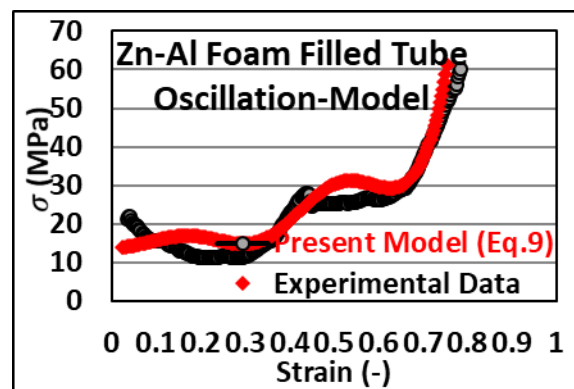
(a)



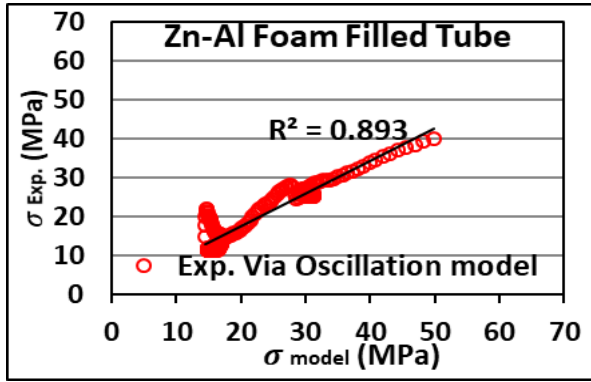
(b)



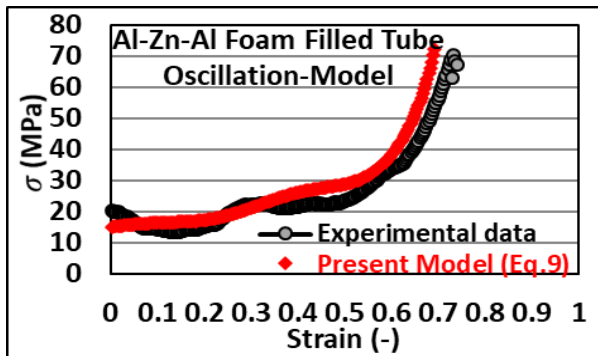
(a)



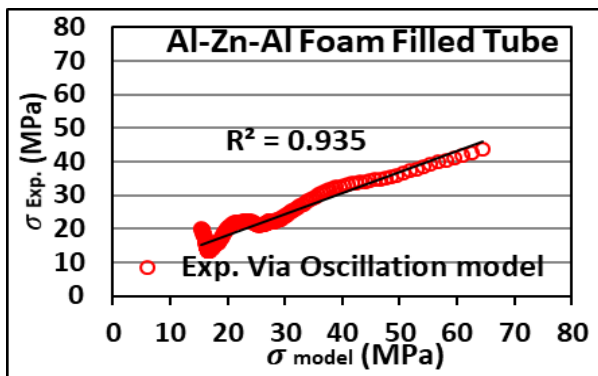
(c)



(d)



(e)



(f)

Fig. 18. Comparison of the stress-strain plots and stress values between the experiment and complementary model for (a, b) Zn foam, (c, d) Zn-Al foam filled tube, (e, f) Al-Zn-Al foam filled tube.

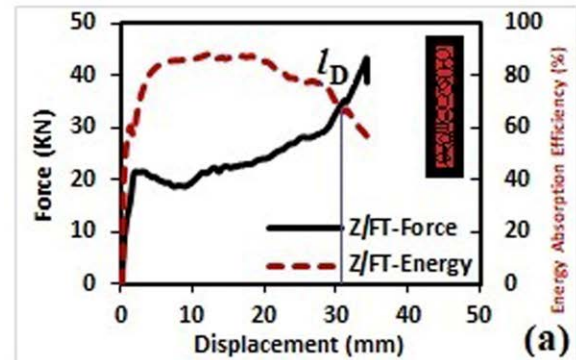
Energy absorption characteristic is an important technological property of the foams and foam filled structures. In this study, E_a and SEA are considered as the most prominent aspects of the evaluation in the energy absorbents. E_a is identified as the total kinetic energy absorbed during the compression test prior to the onset of densification. Therefore, E_a can be calculated by integrating the area under the force-displacement curve up to the densification length (l_D) as follows [2,10]:

$$E_a = \int_0^{l_D} F(x)dx \quad (10)$$

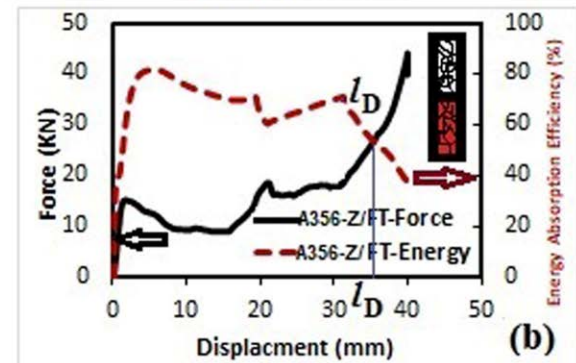
where l_D is measured by the efficiency (η) definition, which is the ratio between the absorbed energy of the real material and ideal absorbent. η (l) is calculated for all points on the force-displacement curve using the following equation [1, 2, 8, 10]:

$$\eta(l) = \frac{\int_0^{l_D} F(x)dx}{\max_{0 \leq x \leq l} F \times l} \quad (11)$$

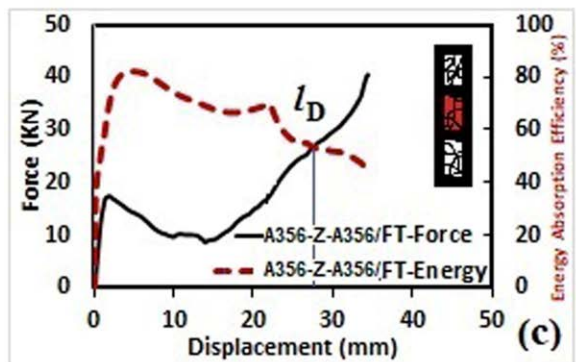
Then, the efficiency is plotted against displacement by employing Eq. (11) on the force-displacement plots, as shown in Fig. 19(a), (b) and (c) for Zn/FT, Al-Zn/FT and Al-Zn-Al/FT, respectively. Finally, the intersection of the force-displacement and efficiency-displacement plots is defined as l_D .



(a)



(b)



(c)

Fig. 19. Force-displacement and efficiency-displacement plots during the compression test for (a) zinc, (b) A356-zinc and (c) A356-zinc-A356 foam filled tubes.

Figure 20 shows the E_a of energy absorbing elements calculated based on Eq. [10] and measured l_D values. Moreover, the SEA parameter, which provides a criterion for the comparison of energy absorbers with different masses or densities, can be calculated as follows [11,13]:

$$SEA = \frac{\int_0^{l_D} F(x)dx}{\rho} \quad (12)$$

where ρ is ρ_F for metallic foams and ρ_{EF} for graded foam filled tubes. The SEA of energy absorbers calculated based on Eq. (12) are reported in Fig. 21. Zn/FT reveals the maximum E_a (581 J) due to the highest density and strength of the zinc foam compared to the A356 foam or layered filler materials considering the same dimensions and geometry of the tube. The SEA is affected by both E_a and ρ of the structure. The SEA of energy absorbers deteriorates with a significant increase in the foam density. Therefore, the low density A356 foam shows more SEA than the high density zinc foam ($87J/(g/cm^3)$ versus $40.7 J/(g/cm^3)$), and the maximum SEA is achieved in Al/FT ($459.2 J/(g/cm^3)$).

In the case of double-layered foam filled tubes, the calculated E_a and SEA of Al-Zn/FT ($408 J - 231.8 J/(g/cm^3)$) and Zn-Al/FT ($388 J - 220.5 J/(g/cm^3)$) are between the corresponding values of Al/FT ($349 J - 459.2 J/(g/cm^3)$) and Zn/FT ($581 J - 209.7 J/(g/cm^3)$). In fact, the E_a and SEA of single- and multi-layered foam filled tubes are mainly controlled by the density of the constituting foam layers, and the existence of more portions of A356 foam results in smaller E_a and greater SEA . However, a little discrepancy is observed in the triple-layered foam filled tubes. It means that almost small E_a and SEA are found in Al-Zn-Al/FT ($266 J - 186 J/(g/cm^3)$) and Zn-Al-Zn/FT ($192 J - 91.4 J/(g/cm^3)$), which is mainly associated with their small failure strain and ϵ_D in spite of nearly high collapse strength. Therefore, the double-layered structures exhibit superior SEA and crashworthiness over the single-layered zinc and triple-layered foam filled tubes. As a result, the compressive and energy absorption features of multi-layered foam filled tubes can be controlled by changing the number and material of foam layers in a certain geometric structure.

By comparison, Zn/FT shows the highest E_a (581 J), which is 66%, 46% and 154% higher than the mean E_a of single-layered A356, double-layered and triple-layered foam filled tubes, respectively. The highest SEA

($459.2 J/(g/cm^3)$) is obtained in Al/FT, which is 12%, 10% and 23% higher than the mean SEA of single-layered zinc, double-layered and triple-layered foam filled tubes, respectively. Consequently, the zinc foam plays a dominant role in adjusting the crash performance and the deformation behavior of graded structures. Although, the SEA decreases by increasing the volume fraction of zinc foam.

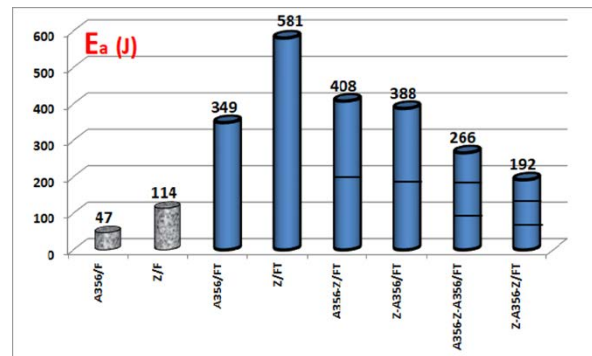


Fig. 20. Total energy absorption results of energy absorbers from the compression tests.

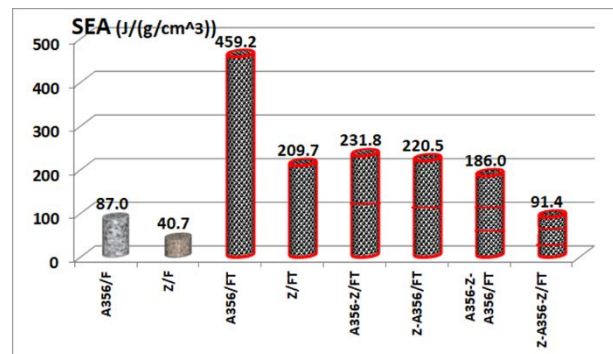


Fig. 21. Specific energy absorption results of energy absorbers from the compression tests.

4. Conclusions

In this study, the strain hardening behavior and energy absorption characteristics of metallic foams and graded foam filled tubes containing one, two or three layers of closed-cell A356 alloy and zinc foams were investigated. The A356 and zinc foams show cell walls' bending and tearing, and thereby partially brittle mechanism in the quasi-static compression test is achieved. The nonlinear asymptotic model, $\sigma = \sigma_0(1 - \epsilon)^{-\rho_F/\rho_S}$, as a function of the relative density, is proposed to represent the hardening behavior of metallic foams and graded foam

filled tubes. Besides, the development of the complementary model, $\sigma = \sigma_0 \varepsilon \sin(n\pi\varepsilon) + \sigma_0(1 - \varepsilon)^{-PF/\rho_s}$, leads to a more accurate estimation of crushing response considering the stress oscillations, particularly for the A356 foam with high degrees of oscillation and multi-layered structures containing distinct plateau regions. Therefore, the present model is in accordance with the experimental results. The higher density and strength of the zinc foam in contrast with the A356 foam result in the highest total energy absorption of the zinc foam filled tube (581 J) and the highest specific energy absorption of the A356 foam filled tube (459.2 J/(g/cm³). The compressive properties of multi-layered structures can be controlled by changing the number and the material of the foam layers at constant geometric features. The zinc foam plays a dominant role in adjusting the crash behavior of graded structures, but the use of A356 foam provides superior specific energy absorption.

Acknowledgments

This work was supported by the Metal Foam Group of Amirkabir University (MFGAU) through Grant No. 110-mir-13951022. The authors are grateful to Rahyaf Advanced Sciences and Technologies Co for their support in casting metal foams.

5. References

- [1] M. G. Nava, A. Cruz-Ramirez, M. A. S. Rosales, V. H. Gutierrez-Perez, A. Sanchez-Martinez: *J. Alloys Compd* 698 (2017) 1009-1017.
- [2] D. K. Rajak, L. A. Kumaraswamidhas, S. Das, S. Senthil Kumaran: *J. Alloys Compd* 656 (2016) 218-225.
- [3] M. A. Islam, A.D. Brown, P. J. Hazell, M. A. Kader, J. P. Escobedo, M. Saadatfar, S. Xu, D. Ruan, M. Turner: *J. Alloys Compd* 114 (2018) 111-122.
- [4] X. Liu, J. Zhang, Q. Fang, H. Wu, Y. Zhang: *Int. J. Impact Eng* 110 (2016) 382-394.
- [5] A. Heydari Astaraie, H. R. Shahverdi, S. H. Elahi: *Trans. Nonferrous Met. Soc. China* 24 (2014) 162-169.
- [6] L. Pan, Y. Yang, M. U. Ahsan, D.D. Luong, N. Gupta, A. Kumar, Predeep K. Rohatgi: *Mater. Sci. Eng., A* 731 (2018) 413-422.
- [7] Y. Sirong, L. Jiaan, L. Yanru, L. Yaohui: *Mater. Sci. Eng., A* 457 (2007) 325-328.
- [8] D. P. Mondal, M.D. Goel, N. Badge, N. Jha, S. Sahu, A.K. Barnwal: *Mater. Des* 57 (2014) 315-324.
- [9] N. Wang, E. Maire, Y. Cheng, Y. Amani, Y. Li, J. Adrien, X. Chen: *Mater. Charact* 138 (2018) 296-307.
- [10] Manoj, D. M. Afzal Khan, D.P Mondal: *Mater. Sci. Eng., A* 731 (2018) 324-330.
- [11] A. G. Hanssen, M. Langseth, O.S. Hopperstad: *Int. J. Impact Eng* 24 (2000) 347-383.
- [12] A. Baroutaji, M. Sajjia, A-G. Olabi: *Thin Walled Struct* 118 (2017) 137-163.
- [13] J. Bi, H. Fang, Q. Wang, X. Ren: *Finite Elem. Anal. Des* 46 (2010) 698-709.
- [14] C. J. Zhang, Y. Feng, X.B. Zhang: *Trans. Nonferrous Met. Soc. China* 20 (2010) 1380-1386.
- [15] M. D. Goel: *Thin Walled Struct* 90 (2015) 1-11.
- [16] Y. Hangai, K. Takahashi, T. Utsunomiya, S. Kitahara, O. Kuwazuru, N. Yoshikawa: *Mater. Sci. Eng., A* 534 (2012) 716-719.
- [17] Y. Hangai, T. Morita, T. Utsunomiya: *Mater. Sci. Eng., A* 696 (2017) 544-551.
- [18] Y. Hangai, Y. Oba, S. Koyama, T. Utsunomiya: *Metall. Mater. Trans. A* 42 (2011) 3585-3589.
- [19] H. Bayani and S.M.H. Mirbagheri: *Iran. J. Mater. Form* 3 (2016) 38-54.
- [20] J. Liu, S. Yu, X. Zhu, M. Wei, Y. Luo, Y. Liu: *J. Alloys Compd* 476 (2009) 220-225.
- [21] S. M. H. Mirbagheri, H. Vali, H. Soltani, Treatment of Closed-Cell A356 + 4 wt.% Cu + 2 wt.% Ca Foam and Its Effect on the Foam Mechanical Behavior, *Journal of Materials Engineering and Performanc* 26 (2017) 14–27.
- [22] N. Movahedi1, S. M. H. Mirbagheri, and S. R. Hoseini, Effect of Foaming Temperature on the Mechanical Properties of Produced Closed-Cell A356Aluminum Foams with Melting Method. *Met. Mater. Int* 20 (2014) 757-763.
- [23] S. Mohammad Hossein Mirbagheri, Mohammad Javad Khajehali, Effect of Fe additive on plastic deformation for crush-boxes with closed-cell metal foams, Part II: Al-Composite Foam-Filled brass tubes Compression Response, *Iran. J. Mater. Form* 1 (2014) 23-31.
- [24] W. F. Hosford, Fundamentals of Engineering Plasticity, Cambridge University Press, London (2013).
- [25] H. Bayani, S. M. H. Mirbagheri, Strain-hardening during compression of closed-cell Al/Si/SiC + (TiB₂ & Mg) foam, *Materials Characterization* 113 (2016) 168-179.

مدلسازی تغییر فرم پلاستیک لوله‌های پر شده با فوم فلزی چند لایه طی بارگذاری فشاری

سید محمدحسین میرباقری، مینا صالحی و امین جعفری رامیانی

دانشکده مهندسی مواد و متالورژی، دانشگاه صنعتی امیرکبیر تهران، تهران، ایران.

چکیده

هدف از پژوهش حاضر بررسی رفتار تغییر فرم پلاستیک و جذب انرژی لوله‌های پر شده با فوم‌های فلزی سلول بسته تک، دو و سه لایه است. فوم‌های فلزی از آلیاژ آلومینیوم A356 و فلز روی خالص هستند که به روش ریخته‌گری تهیه شده بود. نتایج نشان می‌دهد فوم‌های که رفتار غیرترد طی تغییر فرم پلاستیک دارند، منحنی تنش-کرنش آن‌ها از یک نوع تابع نمایی و مجانب‌دار به صورت $\sigma = \sigma_0(1 - \varepsilon)^{-\rho_F/\rho_S}$ پیروی می‌کند. نمای کار سختی این مدل تابع تغییرات چگالی نسبی فوم فلزی به فلز چگال است. اما فوم‌های تک لایه یا چند لایه‌ای که دارای نوسانات طی تغییر فرم پلاستیک هستند از مدل جدید که دارای تابع سینوسی است به صورت $\sigma = \sigma_0 \varepsilon \sin(n\pi\varepsilon) + \sigma_0(1 - \varepsilon)^{-\rho_F/\rho_S}$ پیروی می‌کنند. نتایج جذب انرژی نشان می‌دهد انرژی جذب لوله پر شده با لایه‌های فومی فلز روی به علت دانسیته بالاتر نسبت به A356 بیشتر و برابر ۵۸۱ ژول و انرژی مشخصه آن برابر ۴۵۹ ژول بر چگالی آن است. وجود فوم روی سبب می‌شود انرژی جذب مشخصه سازه فومی کاهش یابد. لذا افزودن فوم روی به عنوان لایه جاذب انرژی در لوله‌های پر شده با فوم فلزی، نقش اصلی را ایفا می‌کند. در سازه‌های جاذب انرژی چند لایه، تعداد لایه‌ها نیز نقش اساسی در نوسانات تغییر فرم پلاستیک طی آزمون فشار دارند.

واژه‌های کلیدی: فوم فلزی، لوله‌های پر شده با هسته‌های فومی چند لایه، تغییر فرم مومسان، جذب انرژی، کار سختی